ISPRS International Journal of

Geo-Information

Article

Land Cover Mapping Analysis and Urban Growth Modelling Using Remote Sensing Techniques in Greater Cairo Region—Egypt

Yasmine Megahed *, Pedro Cabral, Joel Silva and Mário Caetano

NOVA IMS Information Management School, Universidade Nova de Lisboa, Lisboa 1070-312, Portugal; E-mails: pcabral@novaims.unl.pt (P.C.); jsilva@novaims.unl.pt (J.S.); mario@novaims.unl.pt (M.C.)

* Author to whom correspondence should be addressed; E-Mail: m2013313@novaims.unl.pt; Tel.: +2-356-00474.

Academic Editor: Wolfgang Kainz

Abstract: This study modeled the urban growth in the Greater Cairo Region (GCR), one of the fastest growing mega cities in the world, using remote sensing data and ancillary data. Three land use land cover (LULC) maps (1984, 2003 and 2014) were produced from satellite images by using Support Vector Machines (SVM). Then, land cover changes were detected by applying a high level mapping technique that combines binary maps (change/no-change) and post classification comparison technique. The spatial and temporal urban growth patterns were analyzed using selected statistical metrics developed in the FRAGSTATS software. Major transitions to urban were modeled to predict the future scenarios for year 2025 using Land Change Modeler (LCM) embedded in the IDRISI software. The model results, after validation, indicated that 14% of the vegetation and 4% of the desert in 2014 will be urbanized in 2025. The urban areas within a 5-km buffer around: the Great Pyramids, Islamic Cairo and Al-Baron Palace were calculated, highlighting an intense urbanization especially around the Pyramids; 28% in 2014 up to 40% in 2025. Knowing the current and estimated urbanization situation in GCR will help decision makers to adjust and develop new plans to achieve a sustainable development of urban areas and to protect the historical locations.

1. Introduction

Recent studies indicate that our world is undergoing the largest wave of urban growth in history [1]. One hundred years ago, two out of every ten people lived in an urban area, this number is expected to grow to reach six out of ten in 2030, and seven out of ten in 2050 [2]. The world's urban residents began to increase significantly since the 1950s and it is expected to almost double, increasing from approximately 3.4 thousands of million in 2009 to 6.4 thousands of million in 2050 [2]. Consequently, this massive increase in urban population makes governments, policy makers, and civil society organizations face challenges in resources reallocation to overcome the problems that will arise in the future, to achieve a sustainable development of urban areas and to preserve cultural heritage from urban settlements being formed around areas of high legacy.

Models are simplifications of reality; they are theoretical abstractions that represent systems in such a way that essential features crucial to the theory and its application are identified and highlighted [3]. Land Use Land Cover Change (LULCC) models are tools to support the analysis of the causes and consequences of LULCC for a better understanding of the system functionality, and to support land-use planning and policy [4]. Models are useful for simplifying the complex suite of socioeconomic and biophysical forces that influence the rate and spatial pattern of LULCC and for estimating the impacts of changes [4].

Table 1. Different Land Use Land Cover Change (LULCC) models in recent studies.

Model	Study Area	Data Set	Validation Technique	Reference
MC-CA [1]	Harbin, China	Landsat TM 1989, 2007, ETM+2001	Kappa spatial correlation statistic [5]	[6]
LCM	Asmara, Eritrea	Landsat 1989, 2000, 2009	Kappa spatial correlation statistic	[7]
LTM-MC [2]	SEWI [3], USA and MRW [4], Michigan, USA	SEWI and MRW were digitized manually.	ROC [5] [8] and PCM [6] [9,10]	[11]
SLEUTH [7]	Jimei, southeast coast of Fujian Province, China	Landsat TM5 1992, 1997, 2002 and 2007	Lee-Sallee index	[12]

[1] MC-CA: Markov Chain-Cellular Automata; [2] LTM-MC: Land Transformation Model-Multiple Classifications; [3] SEWI: South-Eastern Wisconsin; [4] MRW: Muskegon River Watershed; [5] ROC: Relative Operating Characteristic; [6] PCM: Percent Correct Match; [7] SLEUTH: The name comes from an acronym for the input image requirements for driving the model: Slope, Land use, Exclusion, Urban extent, Transportation and Hill shade [12]

There are four types of modeling approaches: machine learning, cellular sector-based economic, spatially disaggregated economic, and agent-based approaches [13]. Table 1 summarizes some model types in addition to the validation techniques that were applied in some LULCC studies.

Land Change Modeler (LCM) is an integrated software environment for analyzing and predicting LULCC, and for validating the results [14]. It is embedded in the IDRISI software [7], where only thematic raster images with the same land cover categories listed in the same sequential order can be input for LULCC analysis [15]. LCM evaluates land cover changes between two different times, calculates the changes, and displays the results with various graphs and maps. Then, it predicts future LULC maps on the basis of relative transition potential maps [15] relying upon Multi-Layer Perceptron (MLP) neural networks [16]. LCM was found to produce better prediction accuracy in short time scales, especially in the case of stable land covers rather than cases of rapid change [15]. When compared to models that predict LULCC based on supervised approaches (e.g., the Weights of Evidence method, where the weights can be selected and edited by a user), LCM generates more accurate overall change potential maps because neural network outputs are able to express the change of various land cover types more adequately than individual probabilities obtained through the Weights of Evidence method [16].

Different studies have previously been carried out for LULCC detection and modeling in the Greater Cairo Region (GCR). The ISODATA clustering procedure was used for image classification and the image differencing technique was applied to detect the LULCC between 1986 and 1999 [17]. The study indicated that urban areas increased from 344 km^2 in 1986 to 460 km^2 in 1999. Another study applied Maximum Likelihood classifier using ERDAS software for the LULCC detection in 1973 and 2006 [18]. The study applied post-classification comparison techniques for LUCC detection. Results showed that urban areas expanded from 224 km^2 in 1973 to 558 km^2 in 2006, with total agricultural cut-offs and urbanized desert of 137 km^2 and 187 km^2, respectively. The Nearest Distance classifier was used to classify 1984, 2000 and 2008 images, and MC-CA integrated model with Multi Criteria Evaluation procedure was applied in a different study to select and evaluate the driving forces [19]. The model accuracy was 88%, indicating the validity of model parameters, and of the model to predict urban growth for 2038.

This study aims to detect the LULCC from 1984 to 2014, analyze the spatial and temporal growth patterns, and model the changes to predict the LULC in 2025 using LCM.

2. Study Area

The selected area for the study is the metropolitan area of Cairo, the political capital, and Qalyubia, in addition to parts of Giza City that belong to the Greater Cairo Region (GCR) (Figure 1). The study area is located at 30°02'N and 31°21'E, in the middle of the Delta Region, and covers an area of 8942 km^2. Figure 1 shows three 5-km buffer zones around which the urban density will be calculated:

(1) The Great Giza Pyramids and the Sphinx area, representing the Pharaonic history.

(2) Al-Hussien Mosque, Khan Al-Khalily area, Al-Moez Street, and the Citadel, all in one area, representing an essential part of ancient Islamic Cairo.

(3) Al-Baron Palace, which reflects modern Belgian architecture.

The region has the highest population and population density among Egyptian governorates [20], and is considered one of the most populous regions worldwide [20]. The internal migration from Upper Egypt and the Delta began just after the Second World War, especially in the middle of 1950s due to the massive industrialization policy launched by President Nasser, which encouraged people to migrate, seeking better job opportunities and higher quality of education [21]. In 1947, the GCR hosted around three million people, representing 12.5% of the total Egyptian population at the time. This number kept growing to 13 million in 1996, representing 17.3% of the total Egyptian population [21], and, in 2006, it reached 16.1 million people [22]. Cairo City was the most populous among Egyptian cities in 2013, with almost nine million people, representing 10.7% of total population recorded in the same year [20]. Consequently, critical housing pressures began to appear in the GCR [21]. More than 75% of the population is living within only 30 km from the city center, moreover, the region's urban development has been characterized by the rapid expansion of densely populated informal settlements, which reached 40% in 2009 [21].
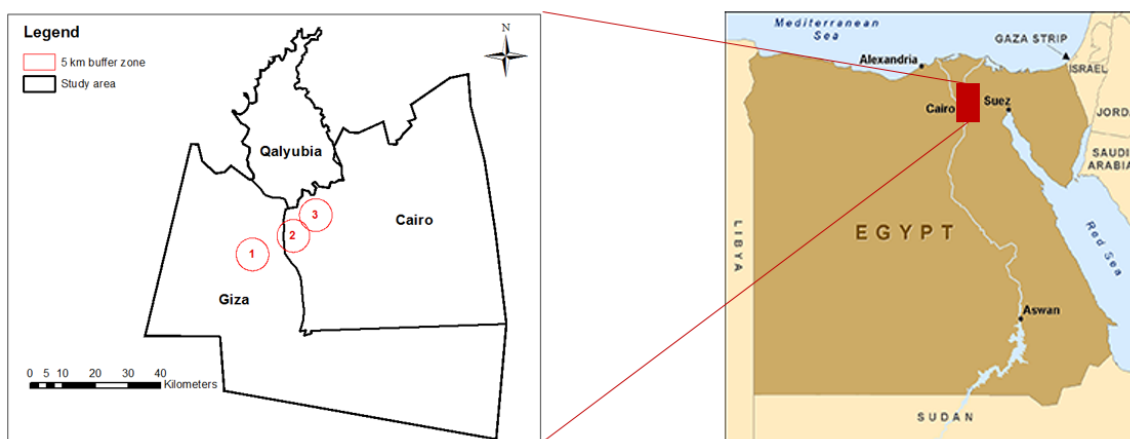

Figure 1. Study area.

On the other hand, the GCR is a land where many civilizations have met over the ages. The Pharaohs, Greeks, Babylonians, Romans, together with Arabs, put it on its way to modernity and enriched the historical value of the city. This diverse historical heritage is facing a threat that is interrelated with urbanization, which requires definitive administrative plans to detect, analyze, and estimate its magnitude and extent. Unfortunately, conventional survey and mapping techniques are expensive and time consuming for urban expansion estimations. Such information is not available for most the urban centers, especially in developing countries [23]. Thus, governmental and private research centers have turned to the use of GIS (Geographic Information Science) and remote sensing tools in monitoring, detecting, and analyzing urban growth [23]. They were found to be cost effective and technologically efficient and, in some cases, they can be the only reliable source of sufficient monitoring [24]. Satellite images provide a synoptic overview for large regions, always recorded with a standardized and calibrated monitoring system [25]. A historic view of the past can usually be viewed for free using image archives that store a large number of satellite remote sensing imagery, starting from the early 1970s, and increase in data daily [25]. These data can be analyzed and used for urban growth prediction and modeling purposes.

3. Data and Methods

3.1. Data

Three cloud free Landsat images for the years 1984, 2003, and 2014 were downloaded at no cost from EarthExplorer [26] (Table 2).

In addition to these datasets, ancillary data were also used: Google Earth maps [27], road networks [28], Digital elevation Model (DEM), and slope [26].

Table 2. Imageries attributes.

Acquisition Date	Sensor	Spatial Resolution	Path/Row	Landsat	Number of Bands	Radiometric Resolution
15/03/2014	OLI-TIRS	30 m	176/39	Landsat 8	11	16 bits
07/07/2003	TM	30 m	176/39	Landsat 5	7	8 bits
02/07/1984	TM	30 m	176/39	Landsat 5	7	8 bits

OLI-TIRS: Operational Land Imager-Thermal Infrared Sensor; TM: Thematic Mapper

3.2. Methodology Overview

Figure 2 illustrates the flowchart of the methodology applied during the study. Multiple satellite scenes for the same study area, obtained at different time stamps (1984, 2003 and 2014), were classified to produce LULC maps. This classification was validated through an accuracy assessment process, which was performed with the aid of validation data or reference maps (e.g., Google Earth maps). The validation was followed by LULCC detection analysis to determine the amount of each class at time t1 that became another class by time t2. These transitions were recorded in a change matrix that represented the input to the subsequent step; calibrating and modeling the transitions of interest. After the driving forces had been set, the transitions between 1984 and 2003 were modeled using LCM to produce a predicted map of 2014. This modeled map was compared to the LULC map of the same year, derived from satellite images, in order to validate the model. Once validated, the model was used with the same prediction time difference (11 years) using the 1984 and 2014 LULC maps to predict the LULC map for 2025.

3.3. LULC Maps Production and LULCC Detection

The three satellite images from 1984, 2003, and 2014 were classified using a SVM classifier. It is a supervised, non-parametric statistical learning approach in which a hyperplane is built to separate examples of different classes, maximizing the distance (margin) of the examples lying close to it [29]. The larger the distances, from the examples of both classes to the hyperplane, are, the better the generalization achieved is [29]. Figure 3 illustrates a simple scenario of a two-class separable classification problem in a two-dimensional input space [30].
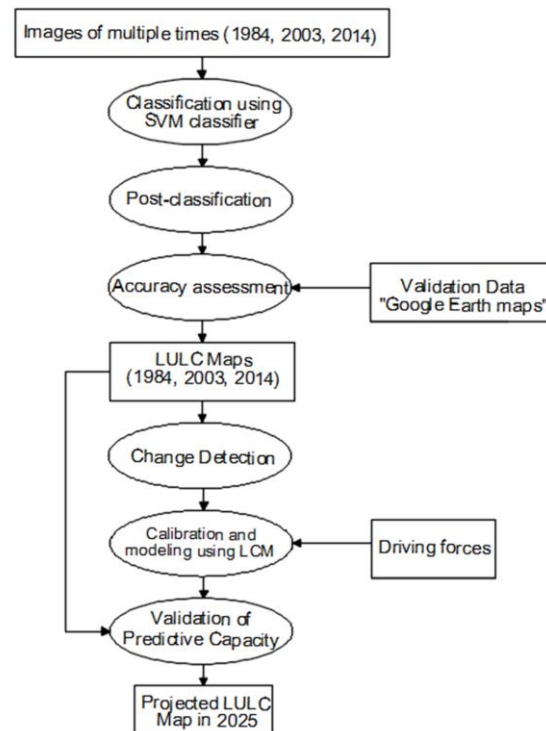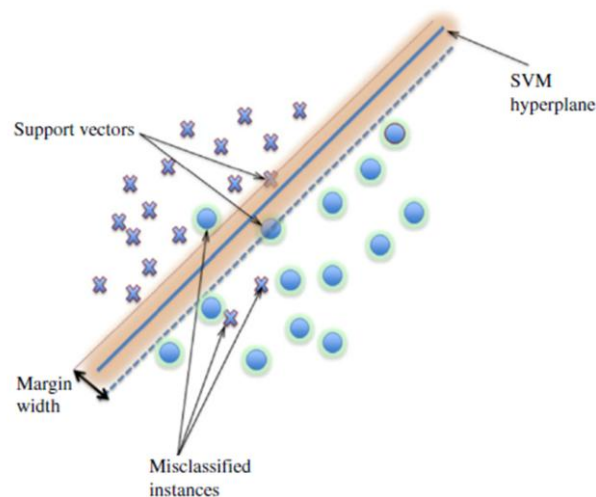
Figure 2. Methodology.

Figure 3. Linear support vector machine example.

SVM represent a noticeable development in machine learning research [31], particularly appealing in the remote sensing field due to is ability to generalize well, even with limited training samples, which is a common limitation for remote sensing applications [30]. It can achieve higher classification accuracy than Maximum Likelihood and Artificial Neural Network [29] with an overall accuracy above 90% [32].

Four LULC classes were considered: Urban, Vegetation, Water, and Desert. In the post-classification step, each raster map was converted to a vector format, and then generalized to a Minimum Map Unit (MMU) of one hectare, by selecting all polygons of an area less than one hectare and eliminating them, to avoid the "salt and pepper" effect so that enhancing the quality of the produced maps to be more representative of the landscape. For accuracy assessment, 100 random points per class were generated over the study area and visually compared to Google Earth images to validate the maps [33]. On the

other hand, for LULCC detection, there are two main groups of change detection techniques: binary change/no-change information, in which the output has only two possibilities; weather the pixel has changed, or not changed, within two specific time stamps [33]. The second approach yields a detailed "from-to" change trajectory, which results in a complete matrix with the exact amount of pixels turned from one class into another (e.g., post classification comparison) [33].

The problem while applying change or non-change detection techniques is the difficulty to precisely identify the thresholds [33]. Usually, methods used to select thresholds lead to external influences on the differences caused by atmospheric conditions, sun angles, soil moistures, and phonological differences, in addition to the threshold itself, is highly subjective and scene dependent, depending on the analyst's familiarity with the study area [33]. The post classification comparison technique consists of an independent classification of each image, followed by a thematic overlay of the classifications, resulting in a complete "from–to" change matrix of the conversion between each class on the two dates [34]. The problem in this technique is the high effect of errors resulting from image classification on the change map. For example, two images classified with 80% accuracy might have only a $0.80 \times 0.80 \times 100 = 64\%$ correct joint classification rate [34].

In the combination of both techniques, the change image is recoded into a binary mask consisting of areas that have changed between the two dates [35]. The change mask is then overlaid onto the second time stamp image and only those pixels that were detected as having changed are classified in the t2 imagery [35]. A traditional post-classification comparison can then be applied to yield complete "from-to" change information. This method may reduce change detection errors. Hence, in this study, a hybrid technique was applied, in which binary maps (areas of change/no-change) for both periods, 1984–2003 and 2003–2014, were produced using the combination of the Normalized Difference Vegetation Index (NDVI), Near Infrared (NIR), and Red differences technique, as it was found that the direct use of NDVI difference, by applying threshold values, failed to detect many urban settlements, while when combined with NIR difference and Red difference, it gave a better result of urban change [36]. Then, only areas of change were thematically overlaid to produce the change matrix in both periods; 1984–2003 and 2003–2014.

3.4. Spatial and Temporal Urban Growth Pattern Analysis

For urban sprawl analysis, FRAGSTATS software, version 4.2, was used to calculate spatial metrics for Urban classes over 30 years, from 1984 to 2014, based on the LULC maps of 1984, 2003, and 2014. The selected subset of matrices applied in the study is given in Table 3. They are the most commonly used and explored metrics in similar studies [37,38].

More complex metrics, such as Area Weighted Mean Patch Fractal Dimension (AWMPFD), Contagion (CONTAG) and Shannon's Entropy were important to be computed for a better understanding of urban sprawl. The fractal dimension describes the complexity and the fragmentation of a patch using a perimeter-area proportion [38]. The values range between 1 and 2, as low values are derived when a patch has a compact rectangular form with a relatively small perimeter compared to the area. If the patches are more complex and fragmented, the perimeter increases and yields a higher fractal dimension [38]. AWMPFD averages the fractal dimensions of all patches by weighting larger land cover patches [38]. CONTAG indicates the heterogeneity of the landscape throughout a given probability that

determines patches adjacency. The lower the CONTAG values are, the more heterogeneous the landscape becomes.

Table 3. Spatial metrics.

Metrics	Description	Units	Range
CA—Class Area	The sum of the areas of all urban patches, that is, total urban area in the landscape.	Hectares	CA > 0, no limit
NP—Number of Patches	The number of urban patches in the landscape.	None	NP ≥ 1, no limit
ED—Edge Density	The sum of the lengths of all edge segments involving the urban patch type, divided by the total landscape area.	Meters/ m²	ED ≥ 0, no limit
LPI—Largest Patch Index	The area of the largest patch of the corresponding patch type divided by total area covered by urban.	%	0 < LPI ≤ 100
ENN_MN—Euclidian Mean Nearest Neighbor Distance	The distance mean value over all urban patches to the nearest neighboring urban patch, based on shortest edge-to-edge distance from cell center to cell center.	Meters	EMN_MN > 0, no limit
AWMPFD—Area Weighted Mean Patch Fractal Dimension	Area weighted mean value of the fractal dimension values of all urban patches, the fractal dimension of a patch equals two times the logarithm of patch perimeter divided by the logarithm of patch area; the perimeter is adjusted to correct for the raster bias in perimeter.	None	1 ≤ AWMPFD ≤ 2
CONTAG—Contagion	Measures the overall probability that a cell of a patch type is adjacent to cells of the same type.	%	0 < CONTAG ≤ 100
Shannon's Entropy	Spatial concentration or dispersion indicator in which lower values imply higher distribution concentration in one region.	None	0 < Shannon's Entropy ≤ 1

4. Model Implementation

LCM embedded in IDRISI 17.0 was used in this study to predict the LULC map in 2025 using the following procedure: change analysis, transition potential modeling and driving forces determination, change prediction, and model validation. In the change analysis step, the changes were assessed between 1984 and 2003. These changes represent the transitions from one class to another, which are important in order to identify the dominant transitions to urban and target them for modeling [39].

4.1. Transition Potential Modeling and Driving Forces Determination

This step is responsible for determining the location of the change [14]. It results in a number of transition potential maps equal to the significant transitions to urban, considered in the change analysis step [14]. These transition potential maps represent the suitability of a pixel to turn into urban one in each transition, based on a group of factors, named "Driving Forces" that are used to model the historical change process. In this study, elevation, slope, distance to roads in 2014, and distance to existing urban

areas in 1984 were set as predictor variables. They were chosen based on recent similar studies [19] in which they were found to highly affect urban sprawl, and were based on the LULCC between 1984 and 2003, where new urban settlements were noticed to occur near the built-up areas and the road network. Distance to urban areas in 1984 was defined as a dynamic factor and was recalculated over the prediction period (11 years, from 2003 to 2014), as an urban area expands, consequently, distance to urban areas in 1984 will vary over time. Likewise, the distance to roads in 2003 should have been considered as a dynamic factor, as new roads are assumed to be built between 2003 and 2014. This could be applied in case the roads were obtained in 2003, but as long as the roads were in 2014, this driving force was set as static.

LCM provides an optional quick test of the potential explanatory power of each driving force represented by Cramer's V. It is a correlation coefficient that ranges from 0.0, indicating no correlation (discarded variable), to 1.0, indicating perfect correlation (excellent potential variable) [14]. Although it does not guarantee a strong performance because it cannot account for the mathematical requirements and the complexity of the relationship [40], it acts as a guide to determine whether the driving force is worth being considered or not [14]. Multi-Layer Perceptron (MLP) neural network is a feedforward neural network in which data flows in one direction from an input layer to an output layer through hidden layer(s) in between [41]. The computing elements (nodes) are grouped into layers and each node receives an input signal from other nodes after processing the signals locally through a transfer function, it outputs a transformed signal to other nodes or final result [42]. Each signal feeding into a node in a subsequent layer has the original input multiplied by a weight with a threshold added and then is passed through an activation function that may be linear or non-linear (hidden units) [42]. The weights have to be determined in the training process before the network can be used for prediction purposes, using part of the data, aiming at changing the weights so as to minimize the error between the observed and the predicted outcomes [42]. A MLP neural network allows for modeling more than one transition at a time [14], hence, it was applied in this study.

4.2. Change Prediction

In this step, LCM uses the change rates calculated from the first step, as well as the transition potential maps produced from the second step, to predict a future scenario for 2014. This step is responsible for determining the quantity of change to urban areas in each transition in 2014 using MC analysis [14]. There are two basic types of predictions: hard and soft predictions [14]. Hard prediction yields a projected map of 2014, where each pixel is assigned one land cover class; the class that it is most likely to become. Soft prediction, however, is different, as it produces a vulnerability map in which each pixel is assigned a value from 0.0 to 1.0, indicating the probability of the pixel to become urban in 2014 [14].

4.3. Model Validation

The validation process aims to determine the quality of 2014's predicted map in relation to 2014's LULC map (the map of what exists in reality). There are two endorsed approaches to validate a model: the visual and the statistical approaches [8]. In the visual validation, a three-way cross tabulation between 2003's LULC map, 2014's predicted map, and the map in reality was run to illustrate the accuracy of the model results. The output is a map that has four categories [8]:

(1) Hits: Model predicted change and it occurred in reality.

(2) False alarms: Model predicted change to urban areas while it persisted in reality.

(3) Misses: Model predicted persistence and it became urban in reality.

(4) Null success: Model did not predict change and it did not occur in reality.

False alarms and misses represent the errors that resulted from the model as a disagreement between the simulated map and the reference map, while hits and null success represent the model correctness [8]. To determine the overall agreement between observed and predicted maps, we calculated the Figure of Merit (FOM), which is a ratio between hits and the summation of hits, misses, and false alarms. It ranges from 0%, meaning no overlap between the observed and predicted change, to 100%, meaning a perfect overlap between the observed and predicted change [43]. On the other hand, the statistical approach examines the agreement between a pair of maps that show any categorical variable, which can have any number of categories [8]. The map of reality acted as the reference map, while the simulated map was the comparison map. In this study, Kappa variations were applied: K_{no} and $K_{localion}$, where K_{no} is the overall accuracy of the simulation run and $K_{localion}$ indicates the level of agreement of location [44]. We eliminated the usage of $K_{standard}$ (the proportion assigned correctly *versus* the proportion that is correct by chance [45]) in this study, as it was not found to be helpful to interpret, while $K_{localion}$ can be somewhat helpful [46]. Once the model predictive power was assessed, it was used to predict 2025's LULC map, with the same driving forces, modeling the changes between 1984 and 2014's LULC maps.

5. Results and Discussion

5.1. LULC Maps Production and LULCC detection

The accuracy assessment resulted in an overall accuracy of 96%, 97.3%, and 96.3%, for 1984, 2003, and 2014's LULC maps (Figure 4), respectively. The most significant changes in both periods (1984–2003 and 2003–2014) are the transitions from vegetation and desert to urban areas. Over 19 years, from 1984 to 2003, vegetation lost 13% to urban, representing 19,179 hectares, and almost the same percentage (12%) within only 11 years, from 2003 to 2014, representing an amount of 16,486 hectares. This indicates the massive leveling of agricultural lands in the GCR for urbanization purposes, especially during the last decade, because of the absence and/or the inactivation of farmland protection laws. Additionally, 3% of desert areas became urban between 1984 and 2003, which is equivalent to 21,417 hectares. This percentage increased to 5% between 2003 and 2014, representing 31,045 hectares, resulting from the application of desert reconstruction strategies to build new communities outside the Nile Valley.

5.2. Spatial and Temporal Urban Growth Pattern Analysis

The temporal urban growth signatures of the spatial metrics are illustrated in Figure 5. As a result of the continuous urban expansion over the study period (1984–2014), CA and NP have boomed between 1984 and 2003 with a dramatic increase in 2014, indicating a higher urbanization rate between 2003 and 2014. ED in 2014 was almost four times of what had been in 1984, thus, indicating an increase in the total length of the edge of the urban patches due to land use fragmentation. Moreover, the increase of LPI emphasizes the proportion growth of the total landscape area comprised by the largest urban patch.

By contrast, ENN_MN dipped from 1984 to 2014, meaning that the space between urban neighbors is shrinking over time as a result of higher urbanization density.

AWMPFD climbed from 1.31 to 1.45 between 1984 and 2003, while, later, it increased steadily to reach 1.46 in 2014. This means that the level of complexity and fragmentation is increasing for the landscape patches. The drop in CONTAG values between 1984 and 2014 may have resulted from higher fragmentation due to more individual urban units. Finally, Shannon's Entropy values have gradually increased over the study period because of the more-dispersed distribution taking place in the GCR.
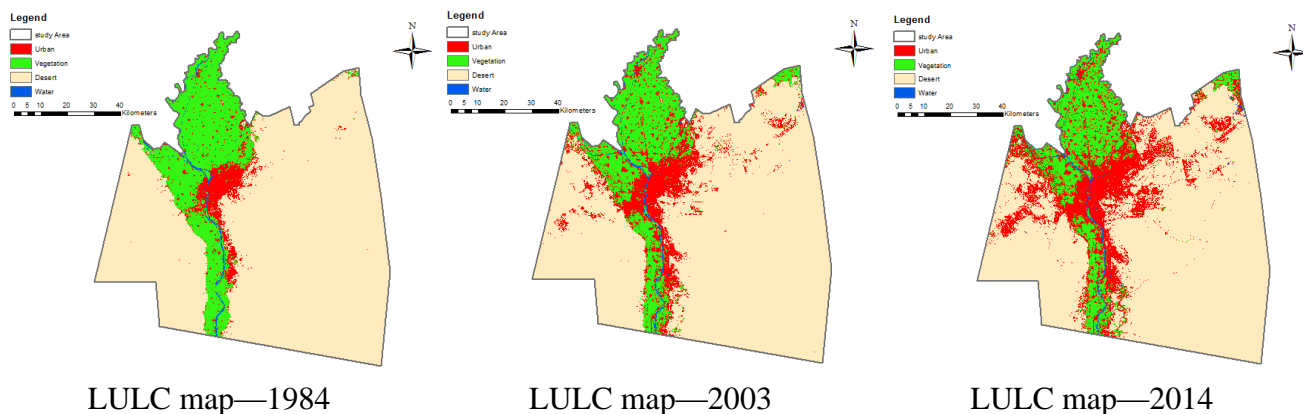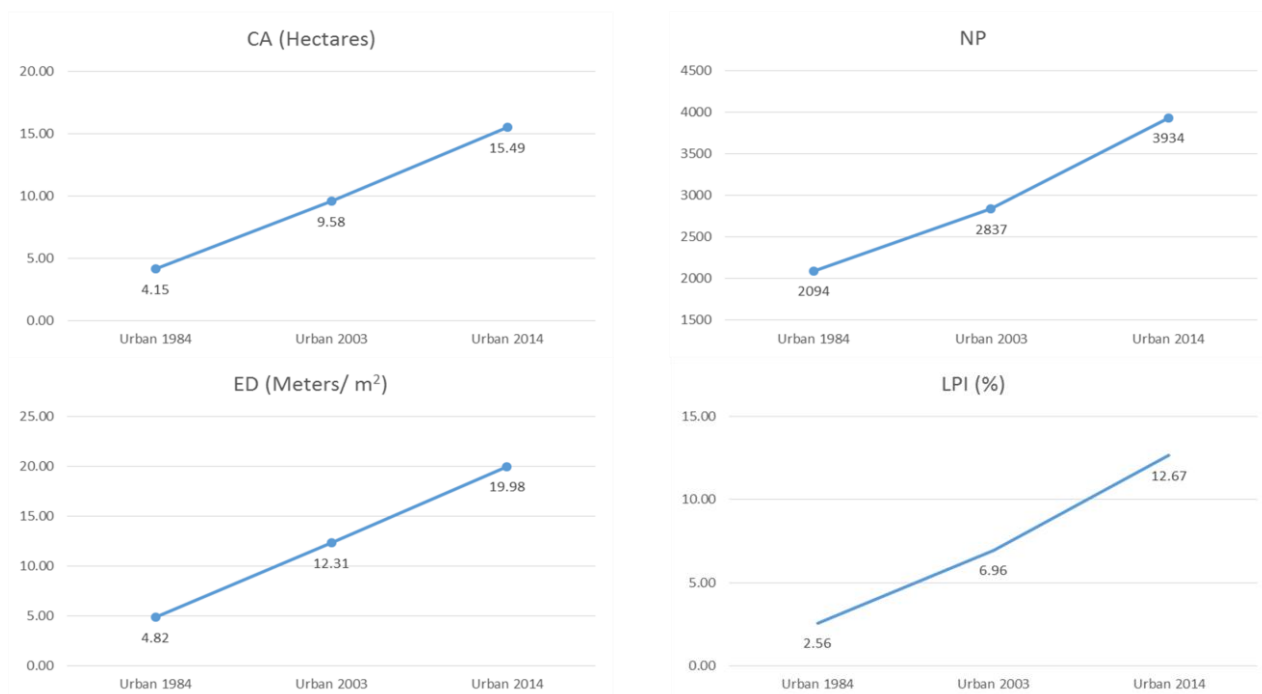
LULC map—1984 LULC map—2003 LULC map—2014

Figure 4. LULC maps.
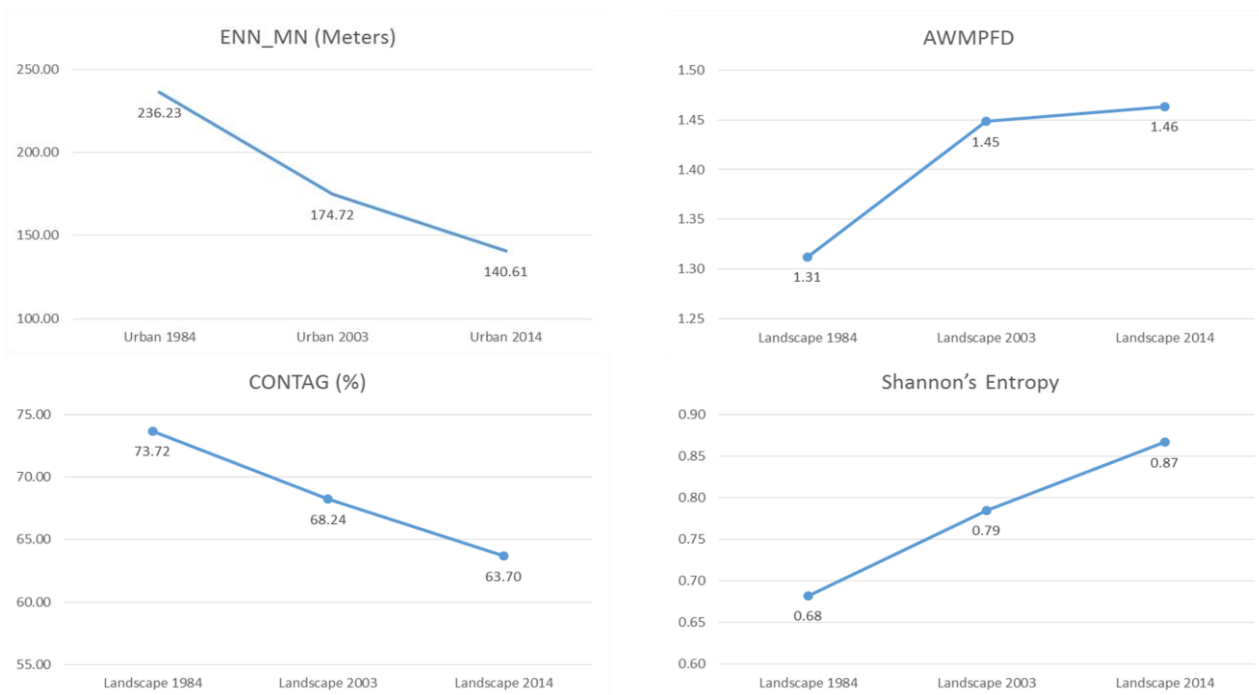
Figure 5. *Cont*.

Figure 5. Temporal urban growth signatures of spatial metrics (Class Area, Number of Patches, Edge Density, Largest Patch Index, Euclidian Mean Nearest Neighbor Distance, Area Weighted Mean Patch Fractal Dimension, Contagion, and Shannon's Entropy).

5.3. Model Implementation

5.3.1. Transition Potential Modeling and Driving Forces Determination

The LULCC results indicated two significant changes to urban areas: from vegetation and from desert, consequently, both were the model's major transitions. Both transitions to urban areas had the same driving forces, depending on the visual examination of the urban spatial trend, which indicated that the selected predictor variables affect both of them. Table 4 illustrates the potential explanatory power of each driving force, represented by Cramer's V. The variables that have a Cramer's V of about 0.15 or higher are useful, while those with values of 0.4 or higher are good [14]. Thus, the selected factors were found to be relevant and worth consideration.

After the selection of the predictor variables, both transitions were modeled in one transition sub-model, as they had the same driving forces, with the aim of producing the transition maps.

Table 4. Cramer's V values of the selected driving forces of change.

Driving Force	Cramer's V
DEM	0.55
Slope	0.49
Distance to roads in 2014	0.25
Distance to urban in 1984	0.52

5.3.2. Model Validation

The visual validation of the simulated change in 2014 resulted in a map of correctness and error, given in Figure 6. The map consists of 1.31% hits, 89.73% null successes, 2.30% false alarms, and 6.66% misses. The simulated change is 3.61% of the landscape, less than the observed change, which is 7.97% of the landscape, and this is why the error occurred. In this case, the FOM is 12.76%, which is a low performance, emphasizing the importance of considering further predictive variables, as is obvious from the results that the applied driving forces are not enough to model this large area of study. Moreover, Figure 6 shows the distribution of the misses, which are highly concentrated in the second transition, from desert to urban, meaning that modeling the urbanization in the desert parts should be done using a set of driving forces different from the set used to model the first transition, from vegetation to urban. Obtaining data about Cairo is always a problematic issue due to the lack of available data and the change of administrative boundaries of the governorates, which yield some areas with no data. The problem is especially highlighted when dealing with a large region like the GCR, where three main cities are included, thus, we were unable to include extra variables in this study (e.g., distance to industrial areas and commercial centers). However, the results are still higher than some recent studies where FOM was 10.4 and 2.9% [39,43]. Although visual examination is the quickest way to reveal spatial patterns, which statistical methods may fail to detect, it is subjective and can be misleading, therefore, the statistical approach is essential [8].
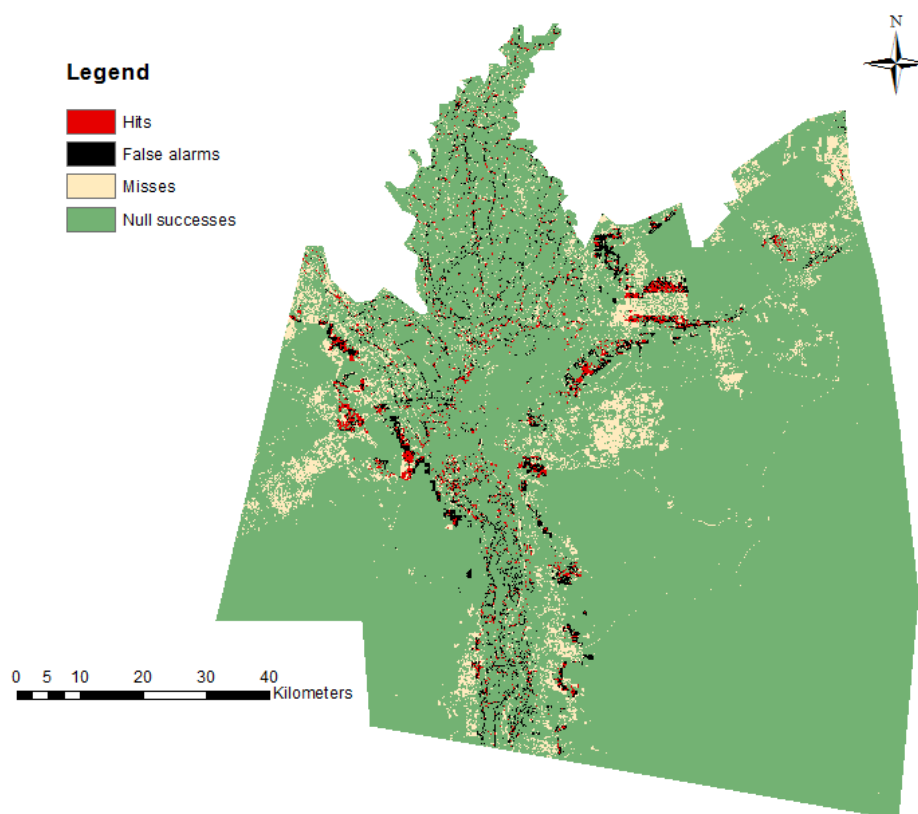

Figure 6. Visual validation—Map of correctness and error based on 2003 (reference), 2014 (reference), and 2014 (simulated) LULC maps.

On the other hand, Kappa variations that compared the projected LULC in 2014 with the actual LULC map in 2014 resulted in K_{no} and $K_{localion}$ of 92.88% and 94.24%, respectively. The interpretation of these high values is that the majority of the study area experienced no change, as, even with the new urban communities that were constructed in the desert areas during the last 30 years (from 1984 to 2014), the desert forms the major land cover that was not subjected to high urbanization during this period. Because of this, it was essential to perform the visual validation throughout the FOM test, as, although Kappa coefficients obtained in this study are above 90%, better than what was obtained in similar studies [47,48], comparing both results reveals the fact that the correct localization of the projected LULCC in areas of change is more pronounced than that in areas of no change. However, Kappa statistic results are more promising than visual validation.

5.3.3. LULC Map Prediction for 2025

The changes between 1984 and 2014 were modeled using the real LULC maps in order to predict the LULC map of 2025 with the same prediction period (11 years). Fourteen percent of the vegetation and 4% of the desert in 2014 are expected to transition to urban areas in 2025, which is equivalent to 16,512 and 24,687 hectares, respectively. Figure 7 shows the urban growth in the GCR in 1984, 2003, 2014, and the estimated urban settlements in 2025. Urban expansion has boomed over 30 years, from 1984 to 2014, and the modeling results confirm that it will be increasing to 2025. The urban areas were 41,488, 95,793 and 154,861 hectares in 1984, 2003, and 2014, representing 4.64%, 10.71%, and 17.32% of the total area of the GCR, respectively. In 2025, according to the model estimations, the urban areas in the GCR will expand to 196,047 hectares, which is about 21.93% of the region. This vast, unplanned growth is a serious threat towards the ecological system, as there is an obvious tendency of a continuous agricultural loss with increasing rates: 13%, 12%, and 14% within 19, 11, and 11 years between 1984–2003, 2003–2014, and 2014–2025, respectively. This implies a current and upcoming threat to the cultural heritage of the GCR, especially with the increasing population in the Egyptian capital.

5.3.4. The Future Effect of Urban Sprawl on the Cultural Heritage

Figure 8 shows the total area of urban settlements within a 5-km buffer around the major monuments previously illustrated in Figure 1. Islamic Cairo and Al-Baron Palace are surrounded by more dense urban areas than the Pyramids' area. In 1984, the Pyramids had almost one-fifth and one-sixth of the urban densities around Islamic Cairo and Al-Baron Palace, respectively, equivalent to 9271 hectares. This value experienced a dramatic increase over time to the extent that it is expected to be equal to the surrounding urban area to the Islamic Cairo in 2025 (70,512 hectares). This calls for preserving plans from the Egyptian policy makers to protect the vital monuments and cultural heritage in the Egyptian capital city.
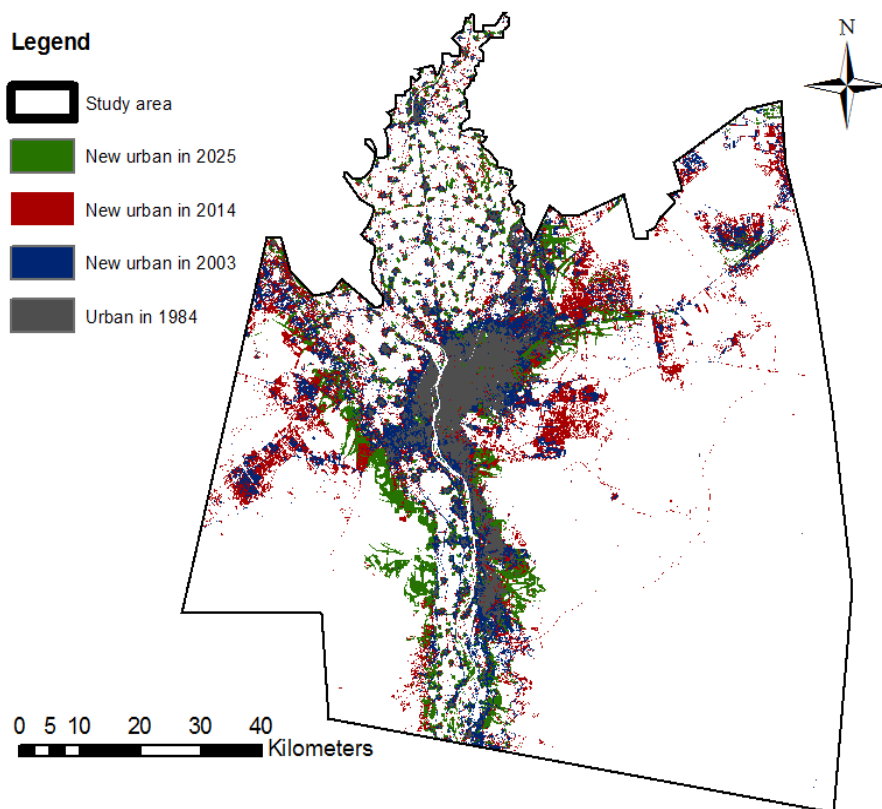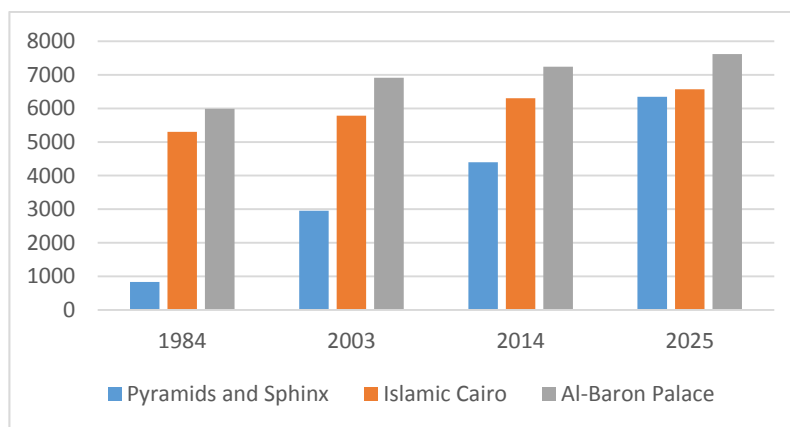
Figure 7. Urban growth in the GCR.

Figure 8. Total area of urban patches within 5-km buffer around cultural monuments (hectares).

6. Conclusions

This study was performed to detect and analyze the urban growth in the GCR over a period of 30 years, from 1984 to 2014, and to model the changes to estimate the urban area in 2025. Three Landsat scenes obtained in 1984, 2003, and 2014 were classified using SVM classifier. LULCC detection was determined using a high-level land-cover mapping-technique, which combines binary maps of change/no-change information with post-comparison approach. From 1984 to 2003, 13% of the vegetation was lost to urban areas, and 12% was lost between 2003 and 2014, representing 19,179 and 16,486 hectares, respectively. While 3% of desert areas became urban between 1984 and 2003,

it increased to 5% between 2003 and 2014, which are equivalent to 21,417 and 31,045 hectares, respectively. The absence of low activation against agricultural land leveling and the application of desert reconstruction strategies, to build new communities outside the Nile Valley, are the main reasons for such massive urbanization.

Eight metrics were computed using FRAGSTATS to analyze the spatial and temporal urban growth, all emphasise the more dense urbanization taking place in the GCR, as well as the dispersed and fragmented landscape as a result of individual urban establishment. The transitions from vegetation and desert to urban were modeled using LCM, with the driving forces: DEM, slope, distance to road network, and distance to existing urban areas. These factors were considered in similar studies and proved to dominate the urbanization for future scenarios. Areas with a high slope clearly represent less of a tendency to become urban [19], and areas of low elevation are most likely to become urban. From the visual inspection of the LULC maps, it was clear that new built-ups tend to be near the existing urban areas and road networks, to make use of the available infrastructures, services, and facilities.

To validate the model, the simulated 2014 map was examined against 2014's real LULC map, applying both visual and statistical approaches, via FOM and Kappa statistics, respectively. Kappa coefficients (K_{no} and $K_{localion}$) were above 90% because the majority of the study area experienced no change, however they are more promising than the FOM, which resulted in 12.76%. The FOM results highlighted the problem of insufficient predicting variables and modeling both transitions (from vegetation and desert to urban) using the same driving forces, as the majority of the misses occurred in the new built-ups in the desert areas. The projected 2025 LULC map estimates an urban transition of 14% from vegetation and 4% from desert, between 2014 and 2025, which are equivalent to 16,512 and 24,687 hectares, respectively.

On the other hand, the areas of urban patches were calculated over time (from 1984 to 2025) in a 5-km buffer around three main historical places in the GCR: the Great Pyramids, Islamic Cairo, and Al-Baron Palace. The results showed similar gradual patterns of urban expansion around Islamic Cairo and Al-Baron Palace, as they both have been surrounded by dense urban settlements. This trend is estimated to continue increasing in 2025 around Al-Baron Palace, whereas no further significant urban development is expected to occur within a 5-km ring around the Islamic Cairo area, as it is already full of urban, showing no promising vacancies for further settlements. However, the Pyramids' area showed a booming urbanization since the urban density in 2014 was five times what it had been in 1984, moreover, this trend is estimated to increase in 2025 to be almost equal to the Islamic Cairo records. These results imply that the Egyptian cultural heritage will be surrounded by urban areas, especially around the Pyramids' area, indicating a gradual loss of value and of its unique appearance. If this trend continues, protection policies have to be undertaken to preserve the cultural heritage and the agricultural fields that will be negatively affected.

Author Contributions

Yasmine Megahed performed all the GIS analyses, processed the data and the model, wrote the paper, and delivered the manuscript. Pedro Cabral contributed to the conception of the research idea, reviewed FRAGSTATS and LCM results, edited and reviewed the overall design. Joel Silva helped in image classification using SVM, as well as image pre- and post-processing. He reviewed the LULC maps and the manuscript. M ário Caetano suggested the hybrid technique that was followed in LULCC detection and reviewed the results related to this part. All authors read and approved the final manuscript.

Conflicts of Interest

The authors declare no conflict of interest.

References

1. United Nations Fund for Population Activities. Urbanization: A Majority in Cities. Available online: http://www.unfpa.org/pds/urbanization.htm (accessed on 23 July 2014).
2. World Health Organization. Urbanization: Urban Population Growth. Available online: http://www.who.int/gho/urban_health/situation_trends/urban_population_growth_text/en/ (accessed on 23 July 2014).
3. Batty, M. Urban modeling. In *International Encyclopedia of Human Geography;* Elsevier: Oxford, UK, 2009; pp. 51–58.
4. Verburg, P.H.; Schot, P.P.; Dijst, M.J.; Veldkamp, A. Land use change modelling: Current practice and research priorities. *GeoJournal* **2004**, *61*, 309–324.
5. Mitsova, D.; Shuster, W.; Wang, X. A cellular automata model of land cover change to integrate urban growth with open space conservation. *Landsc. Urban Plan.* **2011**, *99*, 141–153.
6. Gong, W.; Li, Y.; Fan, W.; Stott, P. Analysis and simulation of land use spatial pattern in Harbin prefecture based on trajectories and cellular automata—Markov modelling. *Int. J. Appl. Earth Obs. Geoinf.* **2015**, *34*, 207–216.
7. Tewolde, M.G.; Cabral, P. Urban sprawl analysis and modelling in Asmara, Eritrea. *Remote Sens.* **2011**, *3*, 2148–2165.
8. Pontius, R.G., Jr.; Chen, H. Land Change Modeling with GEOMOD. Available online: http://planet.botany.uwc.ac.za/nisl/computing/IDRISI_andes/Documentation/Land%20Change%20Modeling%20with%20GEOMOD.pdf (accessed on 15 January 2015)
9. Tayyebi, A.; Pijanowski, B.C.; Pekin, B. Two rule-based urban growth boundary models applied to the Tehran Metropolitan Area, Iran. *Appl. Geogr.* **2011**, *31*, 908–918.
10. Tayyebi, A.; Pekin, B.K.; Pijanowski, B.C.; Plourde, J.D.; Doucette, J.S.; Braun, D. Hierarchical modeling of urban growth across the conterminous USA: Developing meso-scale quantity drivers for the Land Transformation Model. *J. Land Use Sci.* **2013**, *8*, 422–442.
11. Tayyebi, A.; Pijanowski, B.C. Modeling multiple land use changes using ANN, CART and MARS: Comparing tradeoffs in goodness of fit and explanatory power of data mining tools. *Int. J. Appl. Earth Obs. Geoinf.* **2014**, *28*, 102–116.

12. Hua, L.; Tang, L. ; Cui, S.; Yin, K. Simulating urban growth using the Sleuth Model in a coastal peri-urban district in China. *Sustainability* **2014**, *6*, 3899–3914.

13. Brown, D.G.; Walker, R.; Manson, S.; Seto, K. Modeling land-use and land-cover change. In *Land Change Science*; Springer: Houten, The Netherlands, 2004; pp. 395–409.

14. Eastman, J.R. IDRISI Selva Tutorial. Available online: http://uhulag.mendelu.cz/files/pagesdata/eng/gis/idrisi_selva_tutorial.pdf (accessed on 15 December 2014).

15. Roy, H.G.; Dennis, M.F.; Emsellem, K. Predicting land cover change in a Mediterranean catchment at different time scales. In *Computational Science and Its Applications—ICCSA 2014*, Springer International Publishing: Basel, Switzerland, 2014; pp. 315–330.

16. Vega, P.A.; Mas, J.F.; Zielinska, A.L. Comparing two approaches to land use/cover change modelling and their implications for the assessment of biodiversity loss in a deciduous tropical forest. *Environ. Model. Softw* **2012**, *29*, 11–23.

17. Yin, Z.Y.; Stewart, D.J.; Bullard, S.; Maclachlan, J.T. Changes in urban built-up surface and population distribution patterns during 1986–1999: A case study of Cairo, Egypt. *Comput. Environ. Urban Syst.* **2005**, *29*, 595–616.

18. Mohamed, E. Analysis of urban growth at Cairo, Egypt using remote sensing and GIS. *Nat. Sci.* **2012**, *4*, doi:10.4236/ns.2012.46049.

19. de Noronha Vaz, E.; Caetano, M.; Nijkamp, P. Trapped between antiquity and urbanism—A multi-criteria assessment model of the Greater Cairo Metropolitan Area. *J. Land Use Sci.* **2011**, *6*, 283–299.

20. State Information Service. Egypt Gateway. Available online: http://www.sis.gov.eg/En/Default.aspx (accessed on 26 September 2014).

21. Howeidy, A.; Shehayeb, D.K.; Göll, E.; Halim, K.M.A.; Séjourné, M.; Gado, M.; Piffero, E.; Haase-Hindenberg, G.; Löffler, G.; Stryjak, J.; *et al. Cairo's Informal Areas: Between Urban Challenges and Hidden Potentials—Facts, Voices and Visions*; Kipper, R., Fischer, M., Eds.; GTZ Egypt: Cairo, Egypt, 2009.

22. Central Agency for Public Mobilization and Statistics. Available online: http://www.capmas.gov.eg/Default.aspx?lang=2 (Accessed 20 September 2014).

23. Huang, W.; Liu, H.; Luan, Q.; Jiang, Q.; Liu, J.; Liu, H. Detection and prediction of land use change in Beijing based on remote sensing and GIS. *Int. Arch. Photogramm. Remote Sens. Spat. Inf. Sci.* **2008**, *37*, 75–82.

24. Epstein, J.; Payne, K.; Kramer, E. Techniques for mapping suburban sprawl. *Photogr. Eng. Remote Sens.* **2002**, *63*, 913–918.

25. Möller, M.S. Remote Sensing for the Monitoring of Urban Growth Patterns. Available online: http://www.isprs.org/proceedings/XXXVI/8-W27/moeller.pdf (accessed on 10 September 2014).

26. EarthExplorer. Available online: http://earthexplorer.usgs.gov/ (accessed on 20 September 2014).

27. Google Maps. Available online: https://maps.google.com/ (accessed on 20 November 2014).

28. OpenStreetMaps (OSM). Available online: https://www.openstreetmap.org/ (accessed on 20 November 2014).

29. Sáez, J.A.; Galar, M.; Luengo, J., Herrera, F. Tackling the problem of classification with noisy data using multiple classifier systems: Analysis of the performance and robustness. *Inf. Sci.* **2013**, *247*, 1–20.

30. Mountrakis, G.; Jungho, I., Ogole, C. Support vector machines in remote sensing: A review. *ISPRS J. Photogramm. Remote Sens.* **2011**, *66*, 247–259.

31. Pal, M.; Mather, P.M. Support vector machines for classification in remote sensing. *Int. J. Remote Sens.* **2005**, *26*, 1007–1011.

32. Singh, S.K.; Srivastava, P.K.; Gupta, M.; Thakur, J.K., Mukherjee, S. Appraisal of land use/land cover of mangrove forest ecosystem using support vector machine. *Environ. Earth Sci.* **2014**, *71*, 2245–2255.

33. Weng, Q. Remote sensing image classification. In *Advances in Environmental Remote Sensing: Sensors, Algorithms, and Applications*; CRC Press: Boca Raton, FL, USA, 2011.

34. Singh, A. Review article digital change detection techniques using remotely-sensed data. *Int. J. Remote Sens.* **1989**, *10*, 989–1003.

35. Mas, J.F. Monitoring land-cover changes: A comparison of change detection techniques. *Int. J. Remote Sens.* **1999**, *20*, 139–152.

36. Veettil, B.K. A Comparative study of urban change detection techniques using high spatial resolution images. In Proceedings of the 4th GEOBIA, Rio de Janeiro, SP, Brazil, 7–9 May 2012.

37. Araya, Y.H.; Cabral, P. Analysis and modeling of urban land cover change in Setúbal and Sesimbra, Portugal. *Remote Sens.* **2010**, *2*, 1549–1563.

38. Herold, M.; Goldstein, N.C.; Clarke, K.C. The Spatiotemporal form of urban growth: Measurement, analysis and modeling. *Remote Sens. Environ.* **2003**, *86*, 286–302.

39. Olmedo, M.T. C.; Paegelow, M.; Mas, J.F. Interest in intermediate soft-classified maps in land change model validation: Suitability *versus* transition potential. *Int. J. Geogr. Inf. Sci.* **2013**, *27*, 2343–2361.

40. Khoi, D.D., Murayama, Y. Forecasting areas vulnerable to forest conversion in the Tam Dao National Park Region, Vietnam. *Remote Sens.* **2010**, *2*, 1249–1272.

41. Nazzal, J.M.; El-Emary, I.M.; Najim, S.A. Multilayer perceptron neural network (MLPs) for analyzing the properties of Jordan oil shale. *World Appl. Sci. J.* **2008**, *5*, 546–552.

42. Sibanda, W.; Pretorius, P. Novel application of Multi-Layer Perceptrons (MLP) neural networks to model HIV in South Africa using Seroprevalence data from antenatal clinics. *Int. J. Comput. Appl.* **2011**, *35*, 26–31.

43. Rodríguez, N.E.; Armenteras-Pascual, D.; Alumbreros, J.R. Land use and land cover change in the Colombian Andes: Dynamics and future scenarios. *J. Land Use Sci.* **2013**, *8*, 154–174.

44. Nadoushan, M.A.; Soffianian, A.; Alebrahim, A. Predicting urban expansion in Arak Metropolitan Area using two land change models. *World Appl. Sci. J.* **2012**, *18*, 1124–1132.

45. Kim, I.; Jeong, G.Y.; Park, S.; Tenhunen, J. Predicted land use change in the Soyang River Basin, South Korea. In Proceedings of 2011 TERRECO Science Conference, Garmisch-Partenkirchen, Germany, 2–7 October 2011.

46. Pontius, J.; Robert, G., Marco, M. Death to Kappa: Birth of quantity disagreement and allocation disagreement for accuracy assessment. *Int. J. Remote Sens.* **2011**, *32*, 4407–4429.

47. Regmi, R.R.; Saha, S.K.; Balla, M.K. Geospatial analysis of land use land cover change modeling at Phewa Lake Watershed of Nepal by using Cellular Automata Markov Model. *Int. J. Curr. Eng. Tech.* **2014**, *4*, 2617–2627.

48. Subedi, P.; Subedi, K.; Thapa, B. Application of a hybrid cellular automaton-markov (CA-Markov) model in land-use change prediction: A case study of Saddle Creek Drainage Basin, Florida. *Appl. Ecol. Environ. Sci.* **2013**, *1*, 126–132.